

Optimization of scanning Fabry–Perot interferometer in the high spectral resolution lidar for stratospheric temperature detection

Jiawei Qiu,^a Haiyun Xia,^{a,b,c,*} Xiankang Dou,^{a,b} Mingjia Shangguan,^a Chong Wang,^a and Yunpeng Zhang^d

^aUniversity of Science and Technology of China, School of Earth and Space Science, No. 96 Jinzhai Road, Baohe District, Hefei 230026, China

^bChinese Academy of Science, Key Laboratory of Geospace Environment, No. 96 Jinzhai Road, Baohe District, Hefei 230026, China

^cHarbin Institute of Technology, Collaborative Innovation Center of Astronautical Science and Technology, No. 92 Xidazhi Street, Nangang District, Harbin 150001, China

^dTsinghua University, Center for Photonics and Electronics, Department of Precision Instrument, Zhongguancun Street, Haidian District, Beijing 494375, China

Abstract. Although the optimization of a static Fabry–Perot interferometer (FPI)—used as a Doppler shift discriminator in wind lidar—has been proposed, it cannot be applied to the scanning FPI used in the high-spectral resolution lidar for temperature detection. After a comparison, the optimal scanning implementation is chosen and a new optimization scheme is proposed. The free spectral range (FSR) of the FPI is determined by the width of the Rayleigh spectrum. Then, for analytical purposes, the transmission of Rayleigh backscattering through an FPI is simplified to be a superposition of a Gaussian function and a constant background. The maximum likelihood estimation and the Cramer–Rao bound theory are used to derive an analytic expression of the temperature error. Thus, the effective reflectance of the FPI can be optimized. Finally, assuming known atmospheric temperature–pressure–density profiles, backscattering raw signals are simulated using the optimized parameters of the FPI and some other key system parameters of our existing lidar system. Comparisons between the assumed and retrieved temperature profiles revealed that error <2 K can be achieved in the altitude range of 15 to 40 km, even with the disturbance of aerosol contamination. © 2016 Society of Photo-Optical Instrumentation Engineers (SPIE) [DOI: 10.1117/1.OE.55.8.084107]

Keywords: remote sensing and sensors; lidar; Rayleigh scattering; temperature; Fabry–Perot.

Paper 160573 received Apr. 18, 2016; accepted for publication Aug. 2, 2016; published online Aug. 23, 2016.

1 Introduction

The neutral atmospheric temperature profiling techniques are attracting interest for the research of various atmospheric phenomena.^{1,2} Specifically, temperature lidars have shown attractive advantages, such as high accuracy and high spatial and temporal resolutions.³ Generally, the rotational Raman lidar and the Rayleigh integration lidar are the most popular remote sensing techniques for atmospheric temperature profiling in the troposphere and the stratosphere, respectively.^{4,5} Recent research shows that the troposphere influences the stratosphere mainly through atmospheric waves propagating upward. Conversely, the stratosphere organizes the wave forcing up from below to form long-lived changes in its circulation and exerts impact on the tropospheric weather and climate.^{6,7} Thus, accurate temperature profiling is essential to investigate the underlying mechanisms for some phenomena in this region. However, the temperature remote sensing near the altitude of tropopause (which ranges in height from an average of 9 km at the poles to 17 km at the equator) is still a challenging work. On the one hand, the Rayleigh integration lidar is sensitive to the aerosol contamination. Unfortunately, the density of stratospheric aerosols has been increased steadily due to the volcanic eruptions, such as the Pinatubo eruption (in June 1991) and Manam eruption (in January 2005), reaching heights of 34 km.^{8,9} As the aerosol cloud from the volcanic eruptions decays, the aerosol layer has decreased to very low optical depth in the stratosphere but

can still be observed using dual polarization lidar.¹⁰ Ground-based lidars reveal that the stratosphere aerosol load has increased since 2000 at 5% to 7% per year.¹¹ Recent research also shows that volcanic eruptions need not be strong enough to inject sulfur directly to the stratosphere. The SO₂ is lofted into the lower stratosphere by deep convection and the circulation associated with the Asian summer monsoon while converting to sulfate aerosol gradually.¹² Furthermore, the aerosol properties vary quickly in time; the stratospheric aerosol could not be treated as a stable background, and its influence could not be eliminated in the data processing as in the reported Rayleigh integration lidar.⁴ On the other hand, the rotational Raman scattering cross is quite low. Even using a powerful laser, large-area telescope, and sophisticated filters, the signal-to-noise ratio cannot be guaranteed for temperature detection near the altitude of tropopause, especially in day-time operation.¹³

A good solution to the above dilemma is turning to the temperature profiling technique based on the so-called high spectral resolution lidar (HSRL), since the Rayleigh backscattering signal is strong enough in the altitude near 20 km, and the technique is immune to the aerosol contamination.^{14–18} As an example, an HSRL is incorporated into a Rayleigh Doppler wind lidar to eliminate the broadening or narrowing effect of Rayleigh backscattering due to temperature change, which is not accounted for by an edge detection Rayleigh lidar receiver. In the HSRL, the transmission of the Rayl

*Address all correspondence to: Haiyun Xia, E-mail: hsia@ustc.edu.cn

eight backscattering through a Fabry–Perot interferometer (FPI) is obtained by scanning the cavity length of the filter.¹⁹ In fact, a temperature profiling HSRL can also be realized by scanning the frequency of the outgoing laser relative to a static FPI.¹⁴ Recently, the transmission of Rayleigh backscattering is also proposed to be resolved with a Fizeau interferometer and imaging the throughput on a multichannel photomultiplier tube (PMT) array.¹⁴

Compared with the method using scanning FPI, the HSRL with the Fizeau interferometer and multichannel PMT array has its advantages and shortcomings. Although the PMT array can reduce the measurement time,¹⁴ this kind of sampling will cause sampling bias.²⁰ As shown in Fig. 1, the area of the blue bars represents the signal detected by the PMT array, the red dots represent the signal detected by scanning the FPI, and below is the bias of the two implementations. Since the PMT array averages the signal on each channel, the bias can be as large as 0.7%. On the contrary, the detection of the scanning FPI can get the exact intensity of the transmission, which has no bias during the sampling process. Increasing the number of channels in the PMT array will decrease this kind of bias when a Fizeau interferometer is used. However, the cross-talk between the neighboring channels and the anode uniformity of the PMT array will introduce additional system errors. For example, the Licel multispectral lidar detector provides spectral and range resolved data with 32 channels. But the cross-talk between the neighboring channels is 3%, and the anode uniformity can be as large as 1:2.5, which will introduce distortion to the spectrum. What is more, the inactive area between cathodes of the PMT array will waste 20% of the backscattering collected by a telescope. This shortage can be reduced by UV CCD, which samples the Fizeau interferometer fringes with better quantum efficiency, finer spectral resolution, and less cross-talk than a PMT array.²¹ Thus, the scanning FPI method is optimal in our system.

There are also existing HSRL systems using vapor absorption cells to retrieve temperature from the Rayleigh backscattering.^{22–25} Due to the spectral characteristics of absorption lines, the resolution of these systems is coarse, requiring the definition of response functions and calibration procedures, as well as the assumption of hydrostatic equilibrium for temperature retrieval. Furthermore, it is difficult to

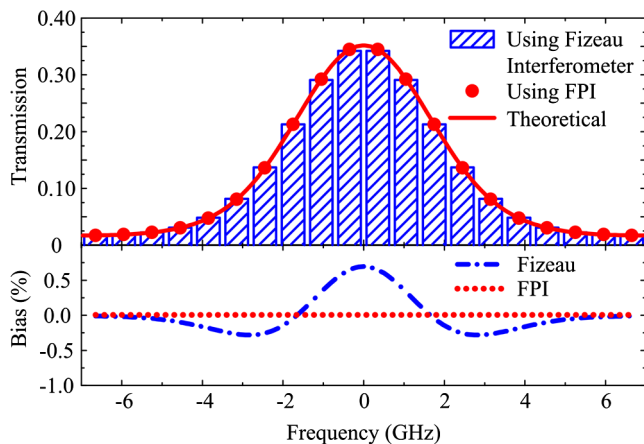


Fig. 1 (a) Sampling of the transmission curve of Rayleigh backscattering through the FPI. (b) Bias between the sampling of PMT array and the correct intensity.

arrange absorption cells for short wavelengths that would be favorable, due to the λ^{-4} proportionality of the Rayleigh backscattering cross section. Operating at UV wavelengths also leaves fewer constraints due to eye safety for ground-, air-, and space-borne lidar operations. In addition, the application of high-resolution interferometers would provide a higher resolution of the RB line shape, leading to better accuracy even with reduced integration time.¹⁴ Thus, the commercially available 355-nm laser and scanning FPI are preferred in our system.

A HSRL based on cavity scanning FPI has been demonstrated for temperature detection from 18 to 50 km.¹⁹ However, this lidar is designed for the stratospheric wind detection and is not so efficient for temperature profiling. To deal with this question, an optimization algorithm is proposed in this work.

The paper is organized as follows. First, the principle of HSRL for temperature profiling is reviewed briefly. Second, an optimization algorithm is introduced, where the key parameters of the FPI are optimized. Third, to evaluate the performance of the HSRL and demonstrate its immunity against aerosol contamination, a simulation is performed. Finally, a conclusion is drawn.

2 Principle

A block diagram of a typical HSRL for temperature profiling is shown in Fig. 2. The outgoing laser is sent to the atmosphere vertically, after passing through a beam expander (transmitter). The atmospheric backscattering is collected and coupled into a transferring fiber by a telescope. The optical signal is then collimated and fed to an FPI. The transmitted backscattering is converted into electrical signal by using a photon detector. Finally, the electrical signal is recorded on a multiscaler (in analog-to-digital or photon-counting model) and processed in a computer. The key instrument in the HSRL system is the scanning FPI.

There are different methods to measure the transmission of backscattering through the FPI, such as scanning the laser frequency relative to the FPI,¹⁴ changing the pressure inside the FPI,^{26,27} and sweeping the cavity length of the FPI. We are focusing on the last method, since we have used it in several Doppler lidars successfully.^{19,28–31} By changing the voltage on the piezoelectric ceramics settled between two mirrors, the cavity length and the parallelism of the FPI can be controlled with high accuracy. It is worth mentioning that the optimization process proposed here is suitable to all the scanning methods reviewed.

The transmission function of an FPI with cavity surfaces parallel to each other perfectly is an Airy function, and a single order of it is approximately a Lorentz function.³² The transmission can also be written in Fourier series as¹⁹

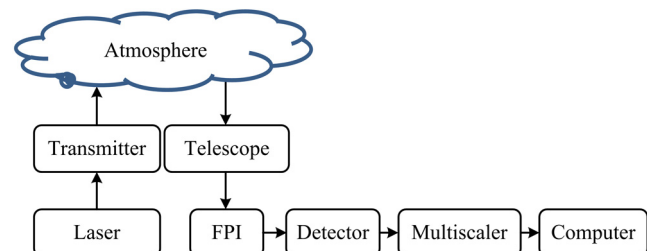


Fig. 2 Block diagram of a typical HSRL for temperature profiling.

$$h(\nu) = T_m \cdot \left\{ 1 + 2 \sum_{n=1}^{+\infty} R_e^n \cos(2\pi n \nu \cdot \cos \theta / \Delta\nu_{\text{FSR}}) \right\}, \quad (1)$$

where R_e is the effective reflectance, ν is the optical frequency relative to the center frequency of the laser (unless otherwise indicated, the frequency mentioned in this paper is the optical frequency relative to the center frequency of the laser), θ is the angle of incidence of the incident light, and $\Delta\nu_{\text{FSR}}$ is the FSR.²¹ $T_m = T_p(1 - R_e)/(1 + R_e)$, where T_p is the peak transmission expressed as

$$T_p = [1 - A_s/(1 - R_e)]^2, \quad (2)$$

and A_s is the absorbance of the surface.

The spectrum of the backscattering is broadened due to the random thermal motions of the air particles. The aerosol backscattering spectrum I_M can be approximated as the spectrum of the outgoing laser I_L , since the Brownian motion of aerosol particles does not broaden the spectrum of Mie backscattering significantly.²⁶ In this work, we focus on the temperature profiling near the tropopause, where the Brillouin scattering is negligible and the molecular motion is thermally dominated.^{33,34} Thus, the backscattering spectrum is a superposition of the Mie backscattering and the Rayleigh backscattering expressed, respectively, as

$$I_M(\nu) \approx I_L(\nu) = (\sqrt{\pi}\Delta\nu_L)^{-1} \exp(-\nu^2/\Delta\nu_L^2), \quad (3)$$

and

$$I_R(\nu) = (\sqrt{\pi}\Delta\nu_R)^{-1} \exp(-\nu^2/\Delta\nu_R^2), \quad (4)$$

where $\Delta\nu_L$ and $\Delta\nu_R$ are the half-width at the $1/e$ intensity level of the laser pulse and the Rayleigh backscattering, respectively. The half-width $\Delta\nu_R$ can be expressed as

$$\Delta\nu_R = (8kT/m\lambda^2)^{1/2}, \quad (5)$$

where k is the Boltzmann constant, T is the atmospheric temperature, m is the average mass of the atmospheric molecules, and λ is the working wavelength. The transmission function of Rayleigh backscattering through a scanning FPI is a convolution of $h(\nu)$, $I_M(\nu)$, and $I_R(\nu)$, which can be expressed as a series:

$$T_R(\nu) = T_m \cdot \left\{ 1 + 2 \sum_{n=1}^{+\infty} \left[R_e^n \cos\left(n\nu\pi \frac{1 + \cos\theta_0}{\Delta\nu_{\text{FSR}}}\right) \cdot \exp\left[\frac{-n^2\pi^2(1 + \cos\theta_0)^2(\Delta\nu_L^2 + \Delta\nu_R^2)}{4\Delta\nu_{\text{FSR}}^2}\right] \cdot \text{sinc}(n\varphi_0) \right] \right\}, \quad (6)$$

where $\varphi_0 = \nu_0(1 - \cos\theta_0)/\Delta\nu_{\text{FSR}}$, ν_0 is the frequency of the laser, and θ_0 is the half-maximum divergence of the collimated beams to the FPI.

Since all the parameters of the FPI and the laser pulse in Eq. (6) can be calibrated with high accuracy in advance, in the temperature profiling experiment, the width of the measured transmission curve is only dependent on the width of the Rayleigh backscattering spectrum (RBS) $\Delta\nu_R$, which is a function of atmospheric temperature. Therefore,

the temperature can be retrieved from the measured transmission of Rayleigh backscattering through the FPI.¹⁹

3 Optimization Algorithm

According to the principles above, the precision of temperature measurement is mainly determined by the FPI. The flowchart of the optimization algorithm of the FPI is shown in Fig. 3, where “Conv.” represents convolution of the three profiles and “ δ_x ” represents the sampling interval. The RBS is obtained by substituting the atmospheric temperature and laser wavelength into Eq. (4). Similarly, the FPI transmission is obtained by substituting the parameters of FPI into Eq. (1). Then, the transmission of Rayleigh backscattering is calculated as a convolution of the laser spectrum, the RBS, and the FPI transmission, resulting a function signed as $T_R(\nu)$ in Eq. (6). However, the function has no analytical expression. For simplicity, first, the $T_R(\nu)$ function is approximated as a superposition of a Gaussian function and a constant background. Second, the sampling interval is determined by setting a sampling bias criterion. Finally, by calculating the temperature error at different effective reflectance of the FPI, the optimized effective reflectance is chosen.

3.1 Model Establishment

The convolution of the laser spectrum, the RBS, and the FPI transmission results in a function $T_R(\nu)$. It has a complex form even expressed as a series form as in Eq. (6), which is not easy for theoretical analysis.

In order to give an analytic expression of the temperature error retrieved from HSRL adopting maximum-likelihood estimation, the function $T_R(\nu)$ is approximated as a superposition of a Gaussian function and a constant background. The error of width estimation of the function $T_R(\nu)$ is assumed equal to the error of width estimation of the Gaussian component in the superposition function.

It is worth noting that an insufficient FSR of the FPI will introduce system error in the temperature detection. The transmission of an FPI is a periodic function; if the FSR is not wide enough relative to the Rayleigh spectrum, the RBS will stretch to the neighboring orders of the FPI during the scanning process. In order to avoid this kind of system error, the FSR is set as 14 GHz at a working wavelength of 355 nm. In this case, the wing intensity of the transmission is nearly zero.

The superposition function of a Gaussian function plus a constant background is expressed as

$$f(x) = A \cdot \exp[-(x - \bar{x})^2/2\omega^2] + B, \quad (7)$$

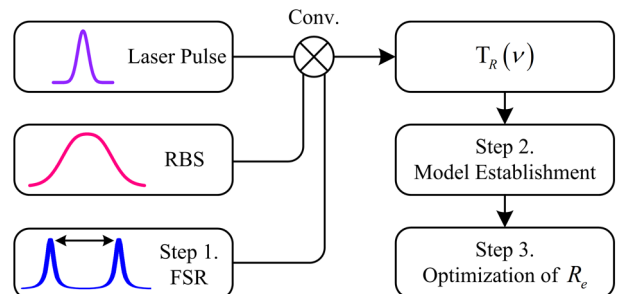


Fig. 3 Flowchart of the proposed optimization algorithm.

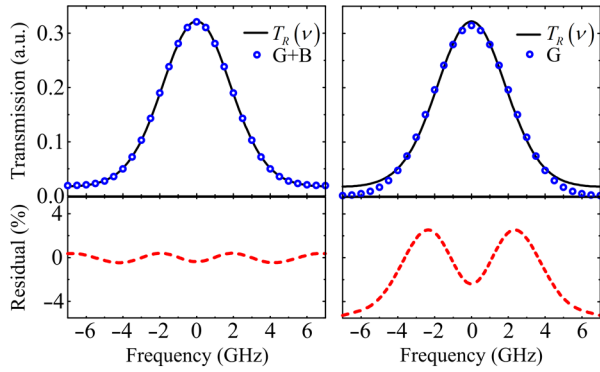


Fig. 4 Approximations of the function $T_R(\nu)$ by two models and the residuals.

where A is the amplitude of the Gaussian function, \bar{x} is the position of the peak, ω is the Gaussian width, and B is the constant background. The approximation of the transmission of Rayleigh backscattering is shown in Fig. 4, where the atmospheric temperature is 300 K, the working wavelength of the laser is 355 nm, and the effective reflectance of FPI is 0.78. One can see that the residual of the approximation by a superposition function of a Gaussian function and a background is smaller than 1%. On the contrary, if the transmission of Rayleigh backscatter is approximated as a Gaussian function, the residual can be as large as 4%.

3.2 Optimization of the Reflectance of the FPI

The finesse of an FPI is a function of the effective reflectance, expressed as

$$F_r = \pi \sqrt{R_e} / (1 - R_e). \quad (8)$$

The optimal effective reflectance can be chosen by calculating the temperature error at different effective reflectances.

The maximum likelihood estimation (MLE) and the Cramer–Rao bound (CRB) theories are used to determine the parameter variances. On the one hand, compared with the least-squares minimization, the MLE provides the minimum-variance unbiased estimate of the parameter set for a large number of measurements. On the other hand, the

$$\mathbf{F} = \delta_x^2 \cdot \begin{pmatrix} \sum S_m E_m^2 & \frac{A}{\omega^2} \sum S_m E_m^2 \xi_m & \frac{A}{\omega^3} \sum S_m E_m^2 \xi_m^2 & \sum S_m E_m \\ \cdots & \frac{A^2}{\omega^4} \sum S_m E_m^2 \xi_m^2 & \frac{A^2}{\omega^5} \sum S_m E_m^2 \xi_m^3 & \frac{A}{\omega^2} \sum S_m E_m \xi_m \\ \cdots & \cdots & \frac{A^2}{\omega^6} \sum S_m E_m^2 \xi_m^4 & \frac{A}{\omega^3} \sum S_m E_m \xi_m^2 \\ \cdots & \cdots & \cdots & \sum S_m \end{pmatrix}, \quad (13)$$

where

$$\left. \begin{aligned} \xi_m &= x_m - \bar{x} \\ E_m &= \exp[-(x_m - \bar{x})^2 / 2\omega^2] \\ S_m &= [\delta_x (A E_m + B)]^{-1} \end{aligned} \right\}. \quad (14)$$

The covariance matrix \mathbf{K} is given by the inverse of the above matrix. Thus, we have the variances of the parameters in Eq. (7) as

CRB provides not just a lower bound on the variance but the variance itself when the number of measurements is sufficient. Thus, the variances of the parameters under estimation can be obtained by using a so-called parameter covariance matrix here rather than using some numerical or Monte Carlo method.³⁵

Under Poisson counting noise, the probability of obtaining photocounts g_m at pixel m is

$$pr(g_m) = \exp(-\bar{g}_m) \cdot \bar{g}_m^{g_m} / g_m!, \quad (9)$$

where $g_m!$ is the factorial of g_m .

The MLE process steps are

1. Construct the likelihood function L :

$$L = pr[\mathbf{g}|\boldsymbol{\theta}] = \prod_{m=1}^M \bar{g}_m^{g_m} / g_m! \cdot \exp(-\bar{g}_m), \quad (10)$$

where $\boldsymbol{\theta} = (A, \bar{x}, \omega, B)$ and M is the number of measurements.

2. Calculate the gradient of the log-likelihood function, often referred to as the “score”:

$$\nabla \ell = \frac{\partial}{\partial \theta_i} \ln L. \quad (11)$$

3. Solve for the parameter set which maximizes the score.

CRB theory states that, when the number of measurements is sufficient, the covariance matrix \mathbf{K} of the parameters is bounded by the inverse of the Fisher information matrix \mathbf{F} : $\mathbf{K} = \mathbf{F}^{-1}$. The Fisher information matrix is relative to the log-likelihood function as

$$F_{ij} = - \int \ell(\boldsymbol{\theta}) (\partial^2 \ell / \partial \theta_i \partial \theta_j) d^M g. \quad (12)$$

Using Eq. (7), we can obtain the symmetric Fisher matrix as in the following equation:

$$\delta A = K_{11}, \quad \delta \bar{x} = K_{22}, \quad \delta \omega = K_{33}, \quad \delta B = K_{44}. \quad (15)$$

The error propagation function of temperature can be derived by Eq. (5) as

$$\delta T = \frac{m\lambda^2}{4k} \cdot \Delta \nu_R \cdot \delta(\Delta \nu_R), \quad (16)$$

where δT is the temperature measurement error and $\delta(\Delta \nu_R)$ is the measurement error of $\Delta \nu_R$. As we recalled

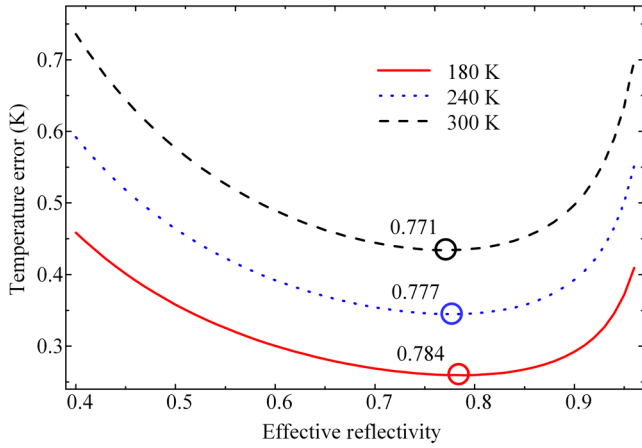


Fig. 5 Atmospheric temperature error versus efficient reflectance at different temperatures.

in the principle section, after careful calibration, the width of the scanned transmission of Rayleigh backscattering through the FPI is only affected by the parameter $\Delta\nu_R$ (the width of RBS). So, the approximation $\delta(\Delta\nu_T) \approx \delta(\Delta\nu_R)$ is assumed here, where $\Delta\nu_T$ is the half-width at the $1/e$ intensity level of the transmission of Rayleigh backscattering and $\delta(\Delta\nu_T)$ is its error. According to the approximation model of the transmission function, Eq. (7), $\Delta\nu_T$ can be expressed as in the following equation:

$$\Delta\nu_T = \omega \left[-2 \ln \left(\frac{A + B - e \cdot B}{A \cdot e} \right) \right]^{1/2}. \quad (17)$$

Therefore, $\delta(\Delta\nu_T)$ can be derived as

$$\delta(\Delta\nu_T) = \frac{\Delta\nu_T \cdot \delta\omega}{\omega} - \frac{\omega^2 (A \cdot \delta B - B \cdot \delta A) \cdot (1 - e)}{A \cdot \Delta\nu_T (A + B - e \cdot B)}. \quad (18)$$

In the simulation, the telescope is pointed vertically to the sky, that is, setting the zenith angle to zero. Considering the

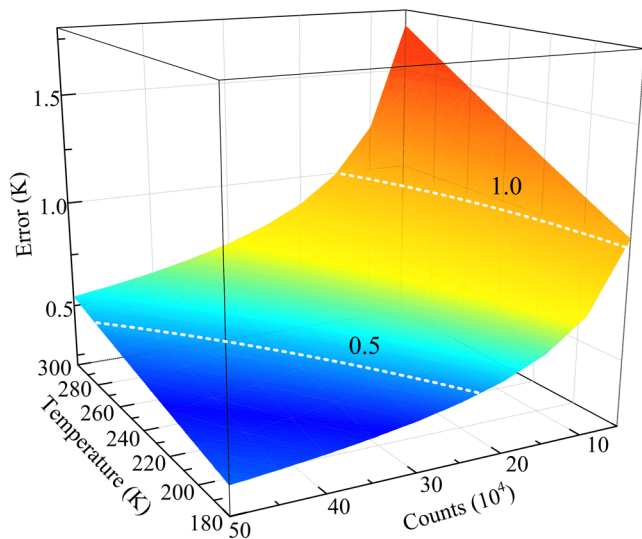


Fig. 6 Temperature error as a function of atmospheric temperature and photon counts arriving at the FPI at each scanning step.

vertical wind speed is in the order of a few centimeters per second, its effect on the temperature detection is ignored in this work.³⁶ Thus, the relation between temperature error and effective reflectance can be carried out, as shown in Fig. 5, where the photon counts arriving at the FPI at each scanning step are set as 400,000. As the atmospheric temperature between 15 and 40 km varies from 210 to 255 K, one can see that an optimized effective reflectance of 0.78 can be chosen. And the width of the Rayleigh transmission shrinks from 4.58 to 3.69 GHz as temperature decreases from 300 to 180 K. The relative change of the FWHM is about 20%, so the resolution increased slightly since the spectrum narrows. One should note that the final width we measured is the transmission of Rayleigh backscatter through the FPI. The temperature error as a function of the atmospheric temperature and the photon counts is also calculated and illustrated in Fig. 6 to estimate the performance of the HSRL technique.

4 Performance Estimation

To evaluate the performance of an HSRL for atmospheric temperature measurement, the analytical detection result is simulated. The key parameters of the optimized HSRL are listed in Table 1; some system characteristics are chosen according to our existing system.¹⁹ The flash-pumped and frequency-tripled Nd:YAG laser (Continuum Model Powerlite 9050) is used in the HSRL system. The PMTs (HAMAMATSU Model R7400P-03) are used for detecting Rayleigh backscattering. Transient recorders (Licel Model TR 20-16bit) are used for signal acquisition, which provide extra dynamic range by employing analog-to-digital detection and single photon counting simultaneously.

The lidar equation used in the simulation is

$$N(\lambda, R) = E \frac{A_0 \xi(R)}{h\nu R^2} \frac{c\tau_L}{2} \xi_R \beta_R(\lambda, R) \cdot T_a^2(\lambda, R), \quad (19)$$

where N is the photocounts detected in the distance of R , λ is the wavelength of the outgoing laser, E is the energy of a laser pulse, A_0 is the area of the telescope aperture, $\xi(R)$ is the overlap factor, ξ_R is the total optical efficiency of the receiver, β_R is the backscattering coefficient of molecular:

$$T_a(\lambda, R) = \exp \left[- \int_0^R \sigma(\lambda, r) dr \right], \quad (20)$$

which is the transmission factor of atmosphere, and σ is the atmospheric attenuation coefficient.³⁷ The transmission of the receiver in Xia’s system can be calculated by the efficiencies listed in Table 1.¹⁹

With the atmospheric parameters extracted from the U.S. standard atmosphere 1976, the intensity and spectra of Rayleigh backscattering at different altitudes can be calculated under clear and hazy weather conditions. According to the raw data in the experiment we carried out at Delhi in 2013, the backscattering photons collected by the telescope at each scanning step using the optimized HSRL can also be calculated, as shown in Fig. 7. The solid line is the simulated photon counts detected under clear weather conditions, the dotted line is under hazy weather conditions, and the dashed line is the simulated photon counts according to the raw data taken at Delhi by Xia on December 23, 2013.¹⁹ The vertical resolutions are set as 100 m in 15 to 20 km, 500 m in 20 to

Table 1 Key parameters of the HSRL.

Instrument parameter	Value
Laser	
Wavelength (nm)	355
1/e width (MHz)	200
Pulse energy (mJ)	250
Pulse repetition rate (Hz)	50
Telescope	
Telescope aperture (mm)	1000
Focal length (mm)	2217
Field of view (mrad)	0.09
Optical efficiency	0.36
Coupling efficiency	0.75
Fiber transmission	0.82
FPI	
FSR (GHz)	14
Effective reflectivity	0.78
FWHM of channels (GHz)	1.5
Sampling interval (MHz)	500
Sampling steps	28
Optics efficiency	0.9
Photomultiplier tube	
Cathode sensitivity (mA/W)	62
Dark counts (c/s)	80
Single photon rise time (ns)	<1.3
Single photon width (ns)	<2.2
Quantum efficiency	0.22
Transient recorders	
ADC resolution (bit)	16
ADC sampling rate (MSamples/s)	20
Bin length (m)	7.5
Max. photon counting rate (MHz)	250

30 km, and 1 km above 30 km. The integration time at each step is set to be 1 min.

The temperature error is estimated in Fig. 8 using the Rayleigh backscattering profile and spectra. The HSRL behaves well in the clear sky model with the error lower than 0.3 K in 15 to 30 km and lower than 1 K in 30 to 40 km. In hazy weather, the max error in the height of 40 km is about 10 K. Temperature errors as large as 10 K

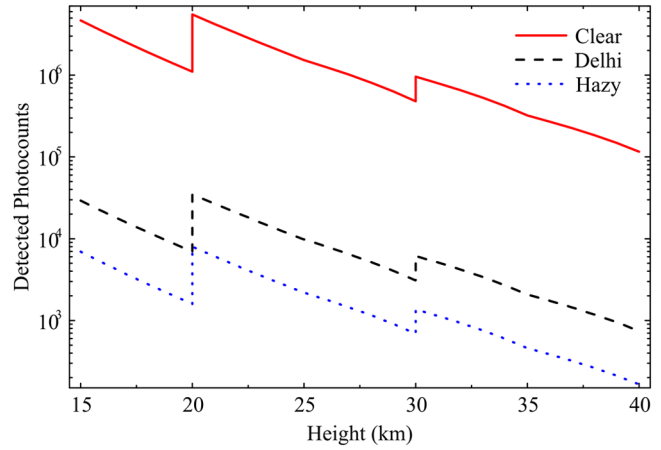


Fig. 7 Simulation results: the backscattering intensity profiles collected by the telescope at each scanning step (before passing through the FPI). The altitude resolution is switched from 100 to 500 m at 20 km and switched from 500 to 1000 m at 30 km.

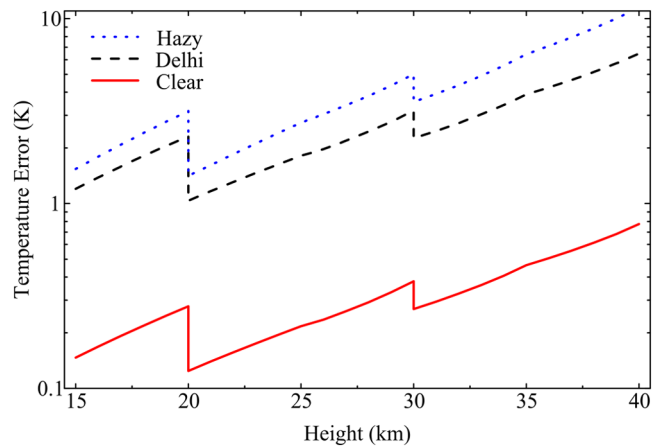


Fig. 8 The simulated temperature measurement error as a function of height.

are inadequate for climatological models. However, since the temperature error is relative to photocounts, as shown in Fig. 6, adaptive accuracy can be realized by changing integration times as well as the range gate extent.

5 Immunity Against Mie Contamination

In the introduction we mentioned that the Rayleigh integration lidar suffers from the disturbance of aerosol contamination in the troposphere and low stratosphere. However, the temperature measurements by HSRL can be compensated for the presence of Mie scattering signals. Furthermore, both aerosol content and temperature measurements are valuable. In order to verify these abilities of HSRL, the immunity for atmospheric temperature profiling against aerosol contamination is demonstrated in the following simulations.

As aerosol contamination is considered, the lidar equation should be updated as

$$N_T(\lambda, R) = E \frac{A_0 \xi(R)}{h\nu R^2} \frac{c\tau_L}{2} \xi_R [\beta_R T_R(\nu) + \beta_M T_M(\nu)] \cdot T_a^2(\lambda, R), \quad (21)$$

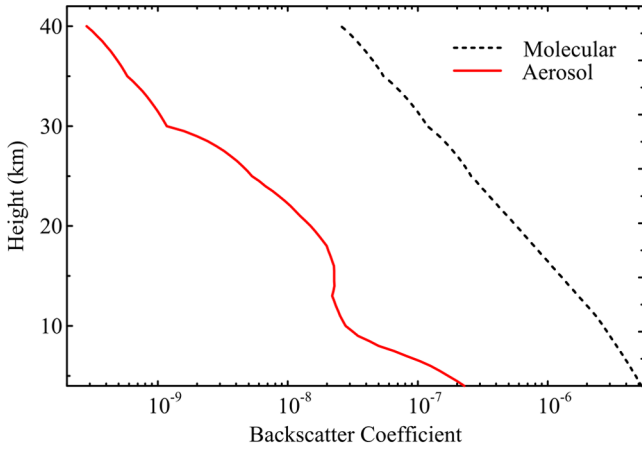


Fig. 9 Rayleigh and Mie backscattering coefficients extracted from the U.S. Standard Atmosphere 1976 under clear weather conditions at 355 nm.

where the transmission of Mie backscattering through the FPI $T_M(\nu)$ can be expressed as

$$T_M(\nu) = T_m \cdot \left\{ 1 + 2 \sum_{n=1}^{+\infty} \left[R_e^n \cos\left(n\nu\pi \frac{1 + \cos \theta_0}{\Delta\nu_{\text{FSR}}} \right) \cdot \exp\left[\frac{-n^2 \pi^2 (1 + \cos \theta_0)^2 \cdot \Delta\nu_L^2}{4\Delta\nu_{\text{FSR}}^2} \right] \cdot \text{sinc}(n\varphi_0) \right] \right\}. \quad (22)$$

The backscattering coefficients of aerosol and molecules β_M and β_R at 355 nm can be calculated, respectively, from the U.S. Standard Atmosphere 1976, as shown in Fig. 9.

Using atmospheric temperature–pressure–density profiles from the U.S. Standard Atmosphere 1976 under clear weather conditions and system parameters, as listed in Table 1, the scanned transmission curves of the atmospheric backscattering through the FPI at different altitudes are simulated using a Monte Carlo computer program, in which the arriving photons follow a Poisson distribution at each scanning step. The integration time at each step is set to be 1 min. The simulation results are plotted at different altitudes, as shown in Fig. 10. Taking advantage of the fact that the Rayleigh backscattering cross section is proportional to λ^{-4} , even the UV working wavelength is used, the superimposed transmission of Mie and Rayleigh through the FPI deviates from the Gaussian function.

Fortunately, by applying a least squares fit procedure to Eq. (22), the atmospheric temperature, Mie backscattering coefficient, and Rayleigh backscatter coefficient can be retrieved simultaneously.^{14,19} As we pointed out in the earlier work, reasonable initial values of parameters under estimation guarantee the convergence of the nonlinear fitting. So, the Klett–Fernald inversion algorithm is suggested to distinguish the Mie backscattering from the Rayleigh backscattering in advance.^{38,39}

In order to illustrate the convergence property of the best fit procedure to Eq. (22), the initial values of the Mie backscattering coefficients are set as 50% and 150% of the assumed known value, which are shown as “Initial Value 1” and “Initial Value 2” in Fig. 11. Then, both Mie backscattering profiles and temperature profiles are compared to the data obtained from the U.S. Standard Atmosphere 1976.

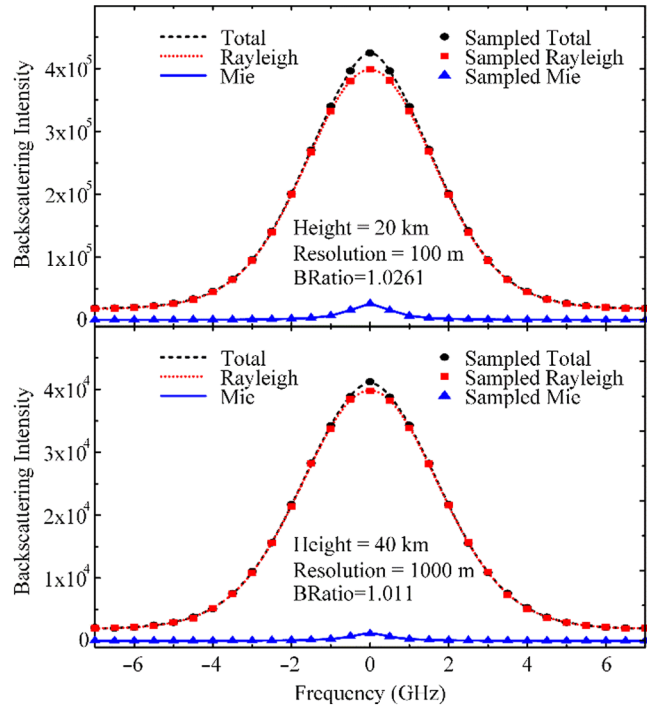


Fig. 10 Simulated photon counts of transmitted backscattering through the FPI. The height resolution is 100 m at 20 km and 1000 m at 40 km. The dashed lines, dotted lines, and solid lines are the ideal signals; the squares, filled circles, and triangles are the simulated photon counts.

The result shows that the retrieved temperature and Mie backscattering profiles match with the assumed known values. In Fig. 11, simulations are performed 40 times at each altitude; then statistics of these data show both the variances of the temperature and Mie backscattering coefficients as plotted as the error bars in the figures. The temperature variances show good agreement with the prediction, as plotted in Fig. 8. Thus, even when poor estimation of the Mie backscattering coefficients is used as the initial value for the best fit, both the temperature and Mie backscattering profiles can be obtained correctly.

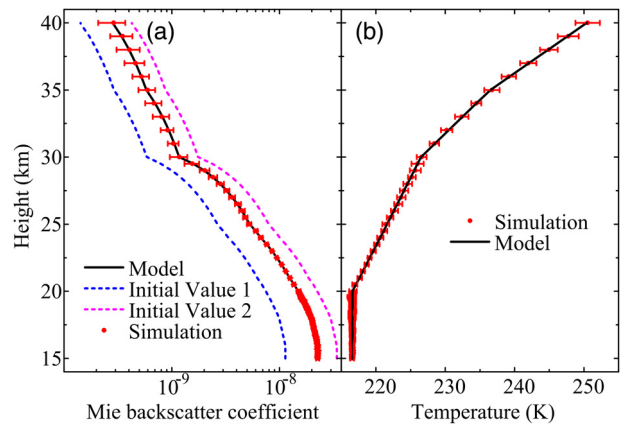


Fig. 11 (a) Simulation of Mie backscattering coefficient (red dot with error bar). The solid line is the coefficients from the atmospheric model, and the blue dotted line and purple dotted line are the initial values of the least squares fitting, which are 50% and 150% of the model. (b) Comparison between the simulated temperature values (red dots with error bar) and the temperature from atmospheric model (solid line).

6 Conclusion

An optimization algorithm was proposed as the guidance for future design of the HSRL for temperature profiling in the altitude near the tropopause. Key parameters, such as the sampling steps, FSR, and effective reflectance of the scanning FPI, were optimized for the operation of the system. Using these optimized parameters and existing system characteristics, one can estimate the performance of the HSRL. Simulations showed that temperature error <2 K can be achieved in the altitude range of 15 to 40 km under clear weather conditions. The immunity of HSRL to the aerosol contamination was also demonstrated.

References

1. J. W. Meriwether and A. J. Gerrard, "Mesosphere inversion layers and stratosphere temperature enhancements," *Rev. Geophys.* **42**, RG3003 (2004).
2. A. J. Gerrard, Y. Bhattacharya, and J. P. Thayer, "Observations of in-situ generated gravity waves during a stratospheric temperature enhancement (STE) event," *Atmos. Chem. Phys.* **11**(22), 11913–11917 (2011).
3. A. Behrendt, "Temperature measurements with lidar," in *Lidar: Range-Resolved Optical Remote Sensing of the Atmosphere*, C. Weitkamp, Ed., pp. 273–305, Springer, Greesthacht, Germany (2005).
4. M. Alpers et al., "Temperature lidar measurements from 1 to 105 km altitude using resonance, Rayleigh, and rotational Raman scattering," *Atmos. Chem. Phys.* **4**, 793–800 (2004).
5. J. Cooney, "Measurement of atmospheric temperature profiles by Raman backscatter," *J. Appl. Meteorol.* **11**, 108–112 (1972).
6. M. P. Baldwin and T. J. Dunkerton, "Stratospheric harbingers of anomalous weather regimes," *Science* **294**(5542), 581–584 (2001).
7. M. P. Baldwin et al., "Weather from the stratosphere?," *Science* **301**(5631), 317–319 (2003).
8. G. Vaughan et al., "Lidar measurements of Mt. Pinatubo aerosols at Aberystwyth from August 1991 through March 1992," *Geophys. Res. Lett.* **21**, 1315–1318 (1994).
9. J.-P. Vernier et al., "Major influence of tropical volcanic eruptions on the stratospheric aerosol layer during the last decade," *Geophys. Res. Lett.* **38**, L12807 (2011).
10. G. Vaughan and D. P. Wareing, "Stratospheric aerosol measurements by dual polarisation lidar," *Atmos. Chem. Phys.* **4**, 2441–2447 (2004).
11. D. Hofmann et al., "Increase in background stratospheric aerosol observed with lidar at Mauna Loa Observatory and Boulder, Colorado," *Geophys. Res. Lett.* **36**, L15808 (2009).
12. A. E. Bourassa et al., "Large volcanic aerosol load in the stratosphere linked to Asian monsoon transport," *Science* **337**(6090), 78–81 (2012).
13. Y. Arshinov et al., "Daytime operation of a pure rotational Raman lidar by use of a Fabry–Perot interferometer," *Appl. Opt.* **44**(17), 3593–3603 (2005).
14. B. Witschas, C. Lemmerz, and O. Reitebuch, "Daytime measurements of atmospheric temperature profiles (2–15 km) by lidar utilizing Rayleigh–Brillouin scattering," *Opt. Lett.* **39**, 1972–1975 (2014).
15. D. Hua, "Ultraviolet high-spectral-resolution Rayleigh–Mie lidar with a dual-pass Fabry–Perot etalon for measuring atmospheric temperature profiles of the troposphere," *Opt. Lett.* **29**, 1063–1065 (2004).
16. D. Hua, M. Uchida, and T. Kobayashi, "Ultraviolet Rayleigh–Mie lidar with Mie-scattering correction by Fabry–Perot etalons for temperature profiling of the troposphere," *Appl. Opt.* **44**, 1305–1314 (2005).
17. D. Liu et al., "Retrieval and analysis of a polarized high-spectral-resolution lidar for profiling aerosol optical properties," *Opt. Express* **21**, 13084–13093 (2013).
18. Z. Cheng et al., "Field-widened Michelson interferometer for spectral discrimination in high-spectral-resolution lidar: practical development," *Opt. Express* **24**, 7233–7245 (2016).
19. H. Xia et al., "Stratospheric temperature measurement with scanning Fabry–Perot interferometer for wind retrieval from mobile Rayleigh Doppler lidar," *Opt. Express* **22**, 21775–21789 (2014).
20. N. Hagen, M. Kupinski, and E. L. Dereniak, "Gaussian profile estimation in one dimension," *Appl. Opt.* **46**, 5374–5383 (2007).
21. O. Reitebuch et al., "The airborne demonstrator for the direct-detection Doppler wind lidar ALADIN on ADM-Aeolus. Part I: Instrument design and comparison to satellite instrument," *J. Atmos. Oceanic Technol.* **26**, 2501–2515 (2009).
22. C. Y. She et al., "High-spectral-resolution Rayleigh–Mie lidar measurement of aerosol and atmospheric profiles," *Opt. Lett.* **17**, 541–543 (1992).
23. Z. Liu et al., "Iodine-filter-based high spectral resolution lidar for atmospheric temperature measurements," *Opt. Lett.* **34**, 2712–2714 (2009).
24. Z. Liu, I. Matsui, and N. Sugimoto, "High-spectral-resolution lidar using an iodine absorption filter for atmospheric measurements," *Opt. Eng.* **38**, 1661–1670 (1999).
25. J. W. Hair et al., "High-spectral-resolution lidar with iodine-vapor filters: measurement of atmospheric-state and aerosol profiles," *Appl. Opt.* **40**, 5280–5294 (2001).
26. C. Souprayen et al., "Rayleigh–Mie Doppler wind lidar for atmospheric measurements. I. Instrumental setup, validation, and first climatological results," *Appl. Opt.* **38**, 2410–2421 (1999).
27. C. Souprayen, A. Garnier, and A. Hertzog, "Rayleigh–Mie Doppler wind lidar for atmospheric measurements. II. Mie scattering effect, theory, and calibration," *Appl. Opt.* **38**, 2422–2431 (1999).
28. H. Xia et al., "Fabry–Perot interferometer based Mie Doppler lidar for low tropospheric wind observation," *Appl. Opt.* **46**(29), 7120–7131 (2007).
29. H. Xia et al., "Mid-altitude wind measurements with mobile Rayleigh Doppler lidar incorporating system-level optical frequency control method," *Opt. Express* **20**, 15286–15300 (2012).
30. M. Shangguan et al., "Comprehensive wind correction for a Rayleigh Doppler lidar from atmospheric temperature and pressure influences and Mie contamination," *Chin. Phys. B* **24**(9), 094212 (2015).
31. R. Zhao et al., "Correction of temperature impact on the wind retrieval from a mobile Rayleigh Doppler lidar," *Chin. Phys. B* **24**(2), 024218 (2015).
32. J. M. Vaughan, *The Fabry–Perot Interferometer: History, Theory, Practice and Applications*, IOP Publishing Ltd, Philadelphia (1989).
33. A. Dabas et al., "Correcting winds measured with a Rayleigh Doppler lidar from pressure and temperature effects," *Tellus A* **60**(2), 206–215 (2008).
34. B. Witschas, C. Lemmerz, and O. Reitebuch, "Horizontal lidar measurements for the proof of spontaneous Rayleigh–Brillouin scattering in the atmosphere," *Appl. Opt.* **51**(25), 6207–6219 (2012).
35. B. J. Rye and R. M. Hardesty, "Discrete spectral peak estimation in incoherent backscatter heterodyne lidar. I. Spectral accumulation and the Cramer–Rao lower bound," *IEEE Trans. Geosci. Remote Sens.* **31**, 16–27 (1993).
36. S. Fukao et al., "Observations of a reversal in long-term average vertical velocities near the jet stream wind maximum," *Mon. Weather Rev.* **119**, 1479–1489 (1991).
37. R. M. Measures, *Laser Remote Sensing (Fundamentals and Applications)*, Chapter 7, p. 243 and Chapter 8, p. 296, Krieger Publishing Company, Florida (1984).
38. F. G. Fernald, "Analysis of atmospheric lidar observations: some comments," *Appl. Opt.* **23**, 652–653 (1984).
39. J. D. Klett, "Lidar inversion with variable backscatter/extinction ratios," *Appl. Opt.* **24**, 1638–1643 (1985).

Jiawei Qiu received his BS degree in geophysics from the University of Science and Technology of China (USTC) in 2014. Now, he is pursuing his PhD in the School of Earth and Space Sciences at USTC. His current research interests include the aerosol lidar, atmospheric temperature lidar, and Doppler wind lidar.

Haiyun Xia received his PhD in optoelectronics from the University of Ottawa and Beijing University of Aeronautics and Astronautics in 2010. He joined the University of Science and Technology of China in 2011 as an associate professor. His current research interests include upconversion technology, superconducting technology, femtosecond laser pulse characterization, Doppler wind lidar, high spectral resolution lidar, and fiber sensors.

Xiankang Dou received his PhD from the University of Paris VII in 1993. Now, he is the vice president of USTC, doctoral supervisor, and professor of geosciences. His current research field includes stratosphere, mesosphere, and lower thermosphere (SMLT) dynamics and waves, laser remote sensing technology, and lidar atmospheric sensing.

Mingjia Shangguan received his BS degree from Jilin University of Architecture in 2012. He is pursuing his PhD in Hefei National Laboratory for Physical Sciences at the Microscale at University of Science and Technology of China. His current research interests include the atmospheric Rayleigh–Brillouin scattering and signal processing.

Chong Wang received his BS degree in optical science and technology from Hefei University of Technology in 2013. He is pursuing his PhD at the University of Science and Technology of China. His current research interests include coherent lidar and atmospheric monitoring.

Yunpeng Zhang received his BS degree in optical science and technology from the University of Science and Technology of China in 2015. He is pursuing his PhD at Peking University. His current research focuses on fiber laser.